

Structural controls on the location of Longqi hydrothermal activity at inside corner revealed by the stress state

Ming Chen

Chunhui Tao

taochunhuimail@163.com

Key Laboratory of Submarine Geosciences, SOA, Second Institute of Oceanography

Yunlong Liu

Hanchuang Wang

Weifang Yang

Kaiying Chen

Mingxu Wang

Dong Liu

Qianyu Li

Dong Chen

Article

Keywords:

Posted Date: May 26th, 2022

DOI: <https://doi.org/10.21203/rs.3.rs-1642852/v1>

License:   This work is licensed under a Creative Commons Attribution 4.0 International License.

[Read Full License](#)

Additional Declarations: There is **NO** Competing Interest.

Version of Record: A version of this preprint was published at Ore Geology Reviews on March 1st, 2024.

See the published version at <https://doi.org/10.1016/j.oregeorev.2024.105938>.

Abstract

The increased hydrothermal activity at inside corners is interpreted to be controlled by the high-permeability detachment faults at mid-ocean ridges. Paradoxically, almost none of hydrothermal activity is confirmed to be located at the detachment terminations, where the permeability is theoretically maximal. Here, we use a numerical model to investigate the stress state of the Longqi hydrothermal field at inside corner, and then explore the structural controls on the hydrothermal activity. The results show that inside corner is undergoing regional stress rotation, deviating from the spreading direction by more than 45°. Shear strain resulting from stress rotation enhances the regional permeability of the shallow crust and therefore might control the location of the hydrothermal site. Our model provides a potential mechanism for hydrothermal activity in similar geological settings where the shear strain enhances regional permeability and facilitates hydrothermal circulation in the hanging wall, and thus reconciles the disparity between prevailing models and field observations.

Introduction

It has long been recognized that on the slow and ultraslow spreading Mid-Ocean Ridges (MORs), the axes are typically divided into distinct accretionary segments by discontinuities, creating fundamental segmentations of the lithosphere plates at a range of scales¹⁻⁵. Inside corners formed either at non-transform discontinuities (NTDs) or at Ridge-Transform Intersections (RTIs) are often associated with increased heat flow and hydrothermal activity⁶⁻⁹. A possible explanation for hydrothermal activity in such settings is that hydrothermal circulation and the generation of the large mineral deposits are dominated by the long-lived, high-permeability detachment fault, which penetrates into Brittle-Ductile Transition (BDT, ~650°C) and allows the hydrothermal fluids to tap heat from a deep reservoir¹⁰⁻¹². Up to now, all the Oceanic Core Complexes (OCCs) that have been explored on the Mid-Atlantic Ridge (MAR) are known to either host active hydrothermal vents or show extinct hydrothermal deposits. Paradoxically, none of the hydrothermal sites is located at the termination of the detachmen¹³, where the permeability is reasonably maximal. In addition, hydrothermal activity is not restricted to the relatively warm segment centers, where the thermal flux is reasoned to be at a maximum^{14,15}. On the contrary, it can equally be located at relatively cold segment ends and discontinuities, which could not be fully explained by previous models.

Constructions of hydrothermal vents require regional permeable pathways and the upwelling of hydrothermal fluids focused at this site. Observations of the Trans-Atlantic Geotraverse (TAG) hydrothermal field, which is located at the hanging wall of a detachment fault, showed that multiple phases of extensional faulting and oblique fractures occurred within the hydrothermal field¹⁶ and the localization of hydrothermal activity seems to be strongly controlled by the permeable pathways^{17,18}. The cause of these oblique faults is most likely not associated with ridge-parallel faults as they deviate from the spreading direction by more than 40°. Up to now, what still remains problematic is the origin of these oblique faults that sustain the upwelling of hydrothermal fluids.

In this paper, we use a numerical model to investigate the present-day stress state of the Longqi hydrothermal field on the ultraslow spreading Southwest Indian Ridge (SWIR). The active Longqi-1 hydrothermal vent (Fig. 1b) is located at the hanging wall of a detachment fault at inside corner and therefore provides an opportunity to explore the possible mechanism for hydrothermal activity in such settings. For comparisons, we estimate stress state of TAG hydrothermal field on the MAR, which is located at a similar geological setting with Longqi field. In contrast to previous models^{19–21}, bathymetry and hydrostatic pressure are coupled in our numerical model in order to investigate the structural controls on the hydrothermal activity, and then understand how a favorable tectonic and volcanic setting may develop for hydrothermal circulation. We will show that shear strain resulting from local stress rotation enhances the regional permeability of the shallow crust and controls the location of the hydrothermal activity.

Geological Setting

The Longqi segment lies at the center of the SWIR (49.3–49.9°E) between Segment 28 and 29, where a ~19.5-km-long NTD is located in between (Fig. 1b). The half-spreading rate is 5.2 mm/y in the north flank and 8.7 mm/y in the south flank, respectively²². The average water depth is shallower in the south flank (< 2000 m) than that in the north flank (> 2000 m). Using the 7.0 km/s isovelocity contour as a reference for the base of the crust, seismic experiments showed that the crustal thickness at inside corner (Fig. 1b) was ~2.0–3.0 km while that at outside corner (Fig. 1b) is 4–5 km^{23,24}. The P-wave velocity at insider corner is ~0.5–2.0 km/s higher than average P-wave velocity in the shallow oceanic crust²⁵. The fraction of the plate separation rate accommodated by magma emplacement, M , is ~0.48²⁶. A possible explanation for the observed structural asymmetry therefore is that nearly all the magmatic accretion occurs in the north flank with small-offset faults while seafloor spreading in the south flank is mainly accommodated by the large-offset detachment fault^{23,24}, as suggested by numerical models^{27–29} and field observations^{10,30}.

The first active, high-temperature Longqi-1 hydrothermal vent field on the SWIR was confirmed during Chinese cruise DY115-19 in 2007³¹. The highest measured temperature of the venting fluid is as high as 350°C¹². Near-bottom magnetic data shows a well-defined low crustal magnetization zone³², which is interpreted be a consequence of hydrothermal alteration. The basalt-hosted Longqi-1 hydrothermal vent is located on the hanging wall of the detachment fault at inside corner. Microearthquake study reveals a relatively uniform BDT base along Longqi segment and adjacent NTD, indicating that no focused melting took place beneath this segment²⁵. Likewise, there is no relatively low-velocity domain beneath the Longqi hydrothermal field²³. Heat source thus would most likely be the melt zone below the Axial Volcanic Ridge (AVR)¹². The detachment fault provides the high-permeability pathway for hydrothermal circulation from upper mantle to the seafloor^{12,23}.

Results

A key point in geomechanical modeling is the reliability of the numerical results in terms of the predicted stress field and mechanical process. Uncertainties are mainly introduced by the model input (e.g. rock properties, boundary conditions and structures). To test the reliability of our model, we compare the present-day stress field predicted by our numerical model with that estimated by model-independent earthquake focal mechanisms. Earthquakes recorded by a sufficient number of stations with a reasonable azimuthal distribution are usually used to estimate focal mechanisms and infer the orientation of the maximum horizontal stress (S_{Hmax})³³⁻³⁵. The focal mechanism database used in this study is obtained from the Global Centroid Moment Tensor Project^{36,37}, where more than 150 stations are available to calculate the stress tensor. The focal mechanisms used in this study are shown in Fig. 2 (beachballs). Table 2 illustrates the comparisons of S_{Hmax} orientation inferred from the focal mechanisms and numerical model, respectively. The maximal difference (C) is 10° and the average difference is $\sim 5^\circ$, suggesting that the orientation of the stress field predicted by numerical model has a good match with the observed. However, it should be noted that the focal mechanisms indicate the stress field at depth of ~ 10 km below seafloor while the numerical results show the present-day stress state of the seafloor.

The orientation and magnitude of the S_{Hmax} predicted by our model are shown in Fig. 2 (black arrows). The magnitude of S_{Hmax} ranges from 15 to 40 MPa and the orientation shows a reasonable correlation with the observed spreading direction. At the inside corner, the S_{Hmax} is rotated by approximate 45° relative to the ridge trend, indicating a strike-slip regime. The magnitude of the shear strain predicted by our model in the study area are shown in Fig. 2b. The magnitude varies from -3×10^{-4} to 3×10^{-4} , where positive values represent the right-moving shearing process and the negative values represent the left-moving shearing process. Similar with the stress field, the distribution of shear strain between the opposite flanks is strongly asymmetric. Shear strain at inside corner is obviously higher than that at outside corner. The red, yellow and black stars represent the active Longqi-1 hydrothermal vent (red star), inactive Longqi-3 hydrothermal field and hydrothermal anomaly.

Discussion

Stress rotation and oblique faults at inside corners

Similar to many other segments on the slow and ultraslow spreading ridges, the Longqi segment are characterized by the strong interplay between tectonic and magmatic processes³⁸. Shipboard bathymetry shows a strong asymmetry between the north and south flank (Fig. 1b). The north flank is characterized by narrow, northward-dipping, axis-parallel normal faults that extend up to 40 km³⁹. The small-offset faults reflect relative rich magma supply²⁷. In contrast, the fault heave and space in the south flank are obviously larger and more spatially complex, reflecting reduced magma supply and stronger interplay between volcanic and tectonic process. In the south flank, seafloor spreading is dominated by the long-lived detachment fault capped by corrugated slip surfaces^{12,23}. Faults at the segment centers strike approximately E-W in respond to extension. At the segment end, however, topographic evidence reveals

the presence of three oblique faults in a NE-SW trend (dashed red lines in Fig. 1b). Applying a selection criterion based on a root mean square fault plane uncertainty of $< 35^\circ$ and a mechanism probability of $> 60\%$, Yu et al. (2018)²⁵ reported two well-constrained earthquake focal mechanisms located ~ 3 km west of the Longqi-1 hydrothermal vent. These events indicate almost N-S-trending fault planes and a strong shear component in the lithosphere. Although the origin of these oblique faults is not clearly understood, we believe the mechanism for the localized strike-slip structures must be likely not as same as that for the ridge-parallel faults as they deviate from the general trend of the spreading axis by more than 40° . A possible explanation for the oblique structures is that the oblique faults are associated with the NTD in the west. Previous studies on the MAR revealed three significant mechanical characters of the NTDs: 1) NTDs are dominated by oblique fault scarps; 2) sustained strike-slip occurs within the NTDs; 3) the geometry of NTDs appears to be unstable⁴⁰⁻⁴². The non-rigid offset represents a rheologically weak plate boundary along which shear stress is accommodated over a broad zone of oblique, normal and strike-slip faulting^{1,43}. Shear deformation at NTDs therefore appears to be accommodated by wide zones (> 10 km) of oblique or ridge-parallel faults instead of the narrow zones (< 5 km).

The Longqi-1 hydrothermal vent field, located at the inside corner, is mapped in higher resolution (Fig. 3). The bathymetric data were collected by the autonomous underwater vehicle Autonomous Benthic Explorer (ABE) and operated by the Woods Hole Oceanographic Institution (WHOI) during the second leg of the Chinese cruise DY115-19 on board R/V DaYangYiHao in 2007³². The depth is ~ 2650 m and its summit is a flat ($\sim 15^\circ$) and corrugated surface, interpreted to be an exhumed detachment surface. More than 20 active and inactive vents were reported based on near-bottom Jiaolong human-occupied vehicle and Qianlong II autonomous underwater vehicle¹². All of these vents are located along the narrow faults (Fig. 3), which are oblique or perpendicular to the spreading axis (Fig. 3f, g) and are restricted within a 0.5-km-wide band near the active vents. We observed a series of ~ 20 -m-high eastward-dipping faults, which strike NNW (Fig. 3) and are located ~ 10 m west of the active vent. The presence of basalt breccias (Fig. 3d) and the oblique faults (Fig. 3g, h) in NE-SW and W-E trend directly observed by deep-tow camera indicates the rotation of the local stress. The distribution of hydrothermal vent sites suggests that hydrothermal fluid should be focused in the shallow crust beneath oblique faults. The location of hydrothermal vents seems to favor an interpretation where the oblique faults enhance the regional permeability of the hanging wall of the detachment fault and further facilitate hydrothermal circulation. Outflow from a conduit with such a narrow linear geometry would probably generate an axisymmetric sulfide deposit, therefore could explain that the hydrothermal vents are located on the both sides of the faults.

Mechanical asymmetry between inside and outside corner

We estimated the present-day stress field of Longqi segment through numerical approaches incorporating bathymetry, material properties and the spreading rate. Our results show a strong asymmetry between inside and outside corners in terms of stress (Fig. 2a) and shear strain (Fig. 2b). The S_{Hmax} is consistent with the observed spreading direction at outside corner. By contrast, at inside corner, the S_{Hmax} is oriented approximately NE-SW, deviating from the ridge trend by more than 45° (Fig. 2a).

Meanwhile, the shear strain at inside corner is significantly higher than that at outside corner. With the distance from the NTD, the orientation of the S_{Hmax} is gradually transformed from a predominantly NE-SW direction to a predominantly N-S direction. At the same time, the shear strain decreased from the segment end to segment center. The deviation of stress orientation and related shear strain are most likely localized because the shear stress regime is restricted at inside corner rather than in the entire south flank. The mechanical effects of the NTD are inferred to be the key drivers of the origin of stress rotation and shear strain at inside corner²¹. In the shear stress regime, due to relatively weak and unstable lithospheric edges along the NTD relative to adjacent segments, stress rotation and inelastic deformation most likely initiates at this weaken zone in response to far-field extension.

Previous field observations and numerical studies have revealed that the asymmetric spreading was controlled by the fraction of magmatic accretion^{27,29,44}. In these models where M is ~ 0.5 , extension at inside corner is mainly accommodated by a long-lived detachment fault. Our results indicate that NTDs plays an important role in the formation of the asymmetric volcanic and tectonic fabrics. The non-rigid NTDs show a weaker resistance to the ridge-normal stress, and thus the locations and structural geometry can adjust relatively easily¹. The imposition of a shear couple across the NTD results in the rotation of local stress field and the resultant oblique tectonic fabrics. Oblique faults at inside corner have also been recognized from bathymetric data on the MAR^{40,45-47} and the Central Indian Ridge²¹.

Comparisons with TAG hydrothermal field

The TAG hydrothermal field located at $26^{\circ}08'N$ on the MAR is one of the best-studied hydrothermal systems to date¹⁸. High-temperature hydrothermal activity is currently focused at the active TAG mound¹⁷. Similar as Longqi-1 hydrothermal field, the active TAG vent is located in the hanging wall at the inside corner (Fig. 2c) and is interpreted to be controlled by the permeable detachment fault¹⁰. The TAG mound is located at the boundary of the extensional zone in the north and the oblique-fissured areas in the south¹⁸. Multiple phases of extensional faulting and oblique fracture occurred within the hydrothermal field¹⁷. Canales et al. (2007)⁴⁹ proposed that the hydrothermal field is located in a high-porosity zone in the hanging wall, where episodic movement along the fault surfaces may lead to the increased permeability of the hanging wall, periodically reactivating the hydrothermal system and contributing to its longevity⁴⁸.

We estimated stress and shear strain field of the TAG hydrothermal field through numerical approaches (Fig. 2c, d). The method is described before and the parameters can be seen in Table.1 in the supplemental material. We do not find focal mechanisms available within the TAG segment on the GCMT. Similar with Longqi segment, our results show a strong mechanical asymmetry between inside and outside corner at TAG segment. Stress rotation occurs at inside corner, deviating from spreading direction by 40° . The active TAG hydrothermal vent is located at the high-strain area, which likely enhances the regional permeability and facilitates hydrothermal circulation at this site. We find the shear strain at TAG segment seems to be more widely spread than that at Longqi segment, both at inside and outside corner.

We infer the difference is likely associated with the geometry and stability of NTD, which should be controlled by local magmatism and spreading rates.

Implications for permeability and hydrothermal activity in the hanging wall

Hydrothermal circulation requires the confluence of a sufficient heat source and adequate permeability⁵⁰. On a global scale, the melt supply to the spreading center is roughly proportional to the spreading rate. However, even in relative terms, the regional variations of the crustal permeability are poorly unconstrained⁵¹. It has been suggested that on slow and ultraslow spreading centers where the magma supply is low, seafloor spreading is dominated by tectonic stretching. The impact of the variations of regional-scale crustal permeability on the hydrothermal circulation could be stronger than heat source⁵².

This study demonstrates a high-shear-strain area at the inside corner (Fig. 2). A recent study¹² shows that the heat source in our study area is probably located at the depth of 13 ± 2 km below the seafloor, and that detachment fault provides a suitable pathway for hydrothermal circulation. The lithosphere-scale interpretation, however, could not fully account for the location of the active Longqi-1 hydrothermal vent and inactive Longqi-3 hydrothermal field, because both of which are located close to the termination of the detachment fault, where the permeability is reasoned to be at a maximum. Our results show that the active Longqi-1 hydrothermal vent as well as TAG hydrothermal vent are located at the area with maximal shear strain. We therefore infer that the location of the hydrothermal vent should simultaneously be affected by the regional permeability of the shallow crust which is likely enhanced due to shear strain. Detachment surface is thought to be at a depth of ~ 1 km beneath the Longqi-1 hydrothermal vent based on seismic observations^{23,25}. The intersection of the oblique faults with detachment fault at depth, coupled with a suitable heat supply extracted by detachment fault, might control the location of the Longqi-1 hydrothermal field (Fig. 4). In the shallow crust, the high-temperature fluids rise vertically due to buoyancy along the permeable oblique faults to the seafloor (Fig. 4). The different stages of hydrothermal activity including active Longqi-1 hydrothermal vent and inactive Longqi-3 hydrothermal field indicate that the location of up-flow zones changes over time in response to the movement of the oblique faults in the specific areas.

Model limitations

It is important to note that our numerical experiments were performed on a small spatial scale with a high resolution, an isotropic layered media and a relatively simple geometry, aiming to model the present-day stress state within a ridge-offset intersection on the MORs. Due to the lack of a depth-dependent rheology and more realistic structure of the faults, our model is limited to completely predict the depth of the shear strain beneath hydrothermal field, which reflects mechanical properties of the lithosphere and the interplay between magmatic and tectonic process. In addition, based on the isotropic media assumption, the horizontal variations of rock properties (e.g. density, cohesion and porosity) are neglected in our model, leading to it is difficult to interpret the variation of the magnitude of stresses. However, combined with field observations, we believe that our model has revealed some key first-order features of the ridge-

offset intersection on the MORs and their mechanical effects on the hydrothermal activity, which might be a useful reference model for future studies.

Conclusions

Combined with bathymetric data and geological observations, our model provides a potential mechanical mechanism for the hydrothermal activity at the inside corner. The main conclusions of this work are as follows:

1. Our model shows that the inside corner undergoes regional stress rotation and shear strain. Stress direction is likely deflected by more than 45°.
2. Shear strain at inside corner, coupled with a suitable heat supply, likely enhances the regional permeability, facilitates hydrothermal circulation and controls the location of Longqi-1 hydrothermal vents.

Methods

To investigate the present-day stress state, we developed a numerical model based on conservation equations using COMSOL Multiphysics 5.4^{53,54}. Assuming that accelerations other than gravity can be neglected²⁰, we solve the force-balance Eq. 5⁵ for absolute stress (no pore pressure):

$$\nabla \cdot \sigma + F_v = 0, (1)$$

where σ is stress tensor, and F_v is body force. The compressive stress here is reckoned to be positive and the tensile stress is negative. We adopt an explicit hybrid finite element approach to solve force-balance equation. According to Hook's Law, the relationship between the stress tensor and strain, ϵ_{ij} , can be described as following:

$$\sigma_{ij} = E\epsilon_{ij}, (2)$$

Where i and j are coordinate indices (x, y, z), and E is the Young's modulus. The shear strain components can be defined as follows:

$$\epsilon_{ij} = \frac{1}{2} \left(\frac{\partial u_i}{\partial x_j} + \frac{\partial u_j}{\partial x_i} \right), (3)$$

Where u is the displacement.

The initial numerical models comprise a 52-km-long, 53-km-wide and ~ 4.5-km-deep domain and a 13-km-long, 13-km-wide and ~ 4.5-km-deep domain, respectively (see in the supplementary materials). The geometry of the top surface in our model is consistent with the seafloor topography at a resolution of ~ 50 m. For simplification, the other surfaces are simulated as planes. The horizontal x axis is parallel to the ridge axis, the horizontal y axis is perpendicular to the ridge axis, and the vertical z axis is directed

downward. In order to eliminate boundary effects, the area of interest (seafloor in our model) is set at a significant distance away from the bottom surface. The minimum and maximum thickness of our models are 2.5 and ~ 4.5 km, respectively.

Our model contains two different stratigraphic layers (Layer A and Layer B). Based on the physical properties model developed by Hyndman and Drury (1976)⁵⁶ and active-source seismic experiments²³. The density of the two layers is measured from the samples⁵⁷. Yang's modules and Poisson's ratio are derived from active-source P-wave velocity data based on empirical equations⁵⁸. The half-spreading rates are loaded on the model edges. Zero-displacement boundary condition is imposed along the x and z direction while along the y direction, both edges are slip-free²¹. The normal stress equals the overburden pressure and shear stress is set to be zero on the bottom surface. The detail parameters of our model are shown in Table 1 in supplementary materials. Hydrostatic pressure (P) is applied to the top surface, as follows:

$$P_{i,j} = \rho_w g z_{i,j}, (4)$$

where P is hydrostatic pressure, ρ_w is the water density, and z is the depth. Acceleration due to gravity (g) is $9.8 \text{ m} \cdot \text{s}^{-2}$.

Data Availability

The focal mechanism data used in this study are supplied in the Supplementary Tables. The bathymetry data of TAG available on GEOMAP app. Bathymetric data of Longqi can be provided upon request by sending an e-mail to the corresponding author (taochunhuimail@163.com).

Declarations

Acknowledgements

This work was supported by, National Natural Science Foundation of China (42127807, 41906071), Scientific Research Fund of the Second Institute of Oceanography, MNR, grand no. SZ2201, Talent Cultivation Project of Zhejiang Association for Science and Technology (SKX201901) and Oceanic Interdisciplinary Program of Shanghai Jiao Tong University (SL2020MS033).

Author contributions

M. C. wrote down the paper. He was principal investigator of the scientific program, codesigned the experiments and set down the conceptual model. C.T. conceived of the project and contributed the interpretation and writing. Y.L. H.W. and W.Y. participated in the interpretation of the results. K.C. and Q. L. participated in setting up model. M.X. and L.L. participated in data collection. D.C. participated in geology interpretation. All authors participated in the review of this manuscript.

Competing interests

The authors declare no competing interests.

References

1. Grindlay, N.R., Fox, P.J. & MacDonald, K.C. Second-order ridge axis discontinuities in the south Atlantic: Morphology, structure, and evolution. *Marine Geophysical Researches* 13(1), 21–49 (1991).
2. Johnson, G. & Vogt, P. Mid-Atlantic Ridge from 47° to 51° North. *GSA Bulletin* 84(10), 3443–3462 (1973).
3. Schouten, H., Klitgord, K.D. & Whitehead, J.A. Segmentation of mid-ocean ridges. *Nature* 317(6034), 225–229 (1985).
4. Tucholke, B.E. & Lin, J. A geological model for the structure of ridge segments in slow spreading ocean crust. *Journal of Geophysical Research Solid Earth* 99(B6), 11937–11958 (1994).
5. Macdonald, K.C., Fox, P.J., Perram, L.J., Eisen, M.F., Haymon, R.M., Miller, S.P., Carbotte, S.M., Cormier, M.H. & Shor, A.N. A new view of the mid-ocean ridge from the behaviour of ridge-axis discontinuities. *Nature* 335(6187), 217–225 (1988).
6. McCaig, A.M., Cliff, R.A., Escartín, J., Fallick, A.E. & MacLeod, C.J. Oceanic detachment faults focus very large volumes of black smoker fluids. *Geology* 35(10), 935–938 (2007).
7. Kelley, D., Karson, J., Blackman, D. et al. An off-axis hydrothermal vent field near the Mid-Atlantic Ridge at 30° N. *Nature* 412, 145–149 (2011).
8. German, C.R. & Parson, L.M. Distributions of hydrothermal activity along the Mid-Atlantic Ridge: interplay of magmatic and tectonic controls. *Earth & Planetary Science Letters* 160(3–4), 327–341 (1998).
9. Li, B., Yang, Y., Shi, X., Ye, J., Gao, J., Zhu, A. & Shao, M. Characteristics of a ridge-transform inside corner intersection and associated mafic-hosted seafloor hydrothermal field (14.0°S, Mid-Atlantic Ridge). *Marine Geophysical Research* 35(1), 55–68 (2014).
10. deMartin, B.J., Sohn, R.A., Canales, J.P. & Humphris, S.E. Kinematics and geometry of active detachment faulting beneath the Trans-Atlantic Geotraverse (TAG) hydrothermal field on the Mid-Atlantic Ridge. *Geology* 35(8), 711–714 (2007).
11. Escartín, J. & Canales, J. Detachments in Oceanic Lithosphere: Deformation, Magmatism, Fluid Flow, and Ecosystems. *Eos, Transactions American Geophysical Union* 92(4), 31–31 (2011).
12. Tao, C., Seyfried, W.E., Lowell, R.P., Liu, Y., Liang, J., Guo, Z., Ding, K., Zhang, H., Liu, J., Qiu, L., Egorov, I., Liao, S., Zhao, M., Zhou, J., Deng, X., Li, H., Wang, H., Cai, W., Zhang, G., Zhou, H., Lin, J. & Li, W. Deep high-temperature hydrothermal circulation in a detachment faulting system on the ultra-slow spreading ridge. *Nature Communications* 11(1), 1300 (2020).
13. Escartín, J., et al. Tectonic structure, evolution, and the nature of oceanic core complexes and their detachment fault zones (13°20'N and 13°30'N, Mid Atlantic Ridge). *Geochemistry Geophysics Geosystems* 18, 1451–1482 (2017).

14. Escartín, J., et al. Globally aligned photomosaic of the Lucky Strike hydrothermal vent field (Mid-Atlantic Ridge, 37°18.5'N): Release of georeferenced data, mosaic construction, and viewing software. *Geochemistry Geophysics Geosystems* 9, 12 (2018).
15. German, C.R., Baker, E.T., Mevel, C., Tamaki, K and the FUJI Science Team. Hydrothermal activity along the southwest Indian ridge. *Nature* 395,490–493 (1998).
16. Humphris, S. E., Herzig, P. M., Miller, D. J., and Shipboard Scientific Party. Proceedings of the ODP, Ocean Drilling Program, College Station, TX, Initial Reports p. 158 (1996).
17. Kleinrock, M.C. & Humphris, S.E. Structural control on sea-floor hydrothermal activity at the TAG active mound. *Nature* 382(6587), 149–153 (1996).
18. Graber, S., Petersen, S., Yeo, I., Sztikar, F., Klischies, M., Jamieson, J., Hannington, M., Rothenbeck, M., Wenzlaff, E., Augustin, N. & Stobbs, I. Structural Control, Evolution, and Accumulation Rates of Massive Sulfides in the TAG Hydrothermal Field. *Geochemistry Geophysics Geosystems* 21(9), e2020GC009185 (2020).
19. Neves, M.C., Bott, M.H. & Searle, R.C. Patterns of stress at midocean ridges and their offsets due to seafloor subsidence. *Tectonophysics* 386(3), 223–242 (2004).
20. Ziegler, M.O., Heidbach, O., Reinecker, J., Przybycin, A.M. & Scheck-Wenderoth, M. A multi-stage 3-D stress field modelling approach exemplified in the Bavarian Molasse Basin. *Solid Earth* 7(5), 1365–1382 (2016).
21. Tyler, S., Bull, J.M., Parson, L.M. & Tuckwell, G.W. Numerical modelling of non-transform discontinuity geometry: Implications for ridge structure, volcano-tectonic fabric development and hydrothermal activity at segment ends. *Earth & Planetary Science Letters* 257(1), 146–159 (2007).
22. Mendel, V., Sauter, D., Jestin, C.R., Patriat, P., Lefebvre, F. & Parson, L.M. Magmato-tectonic cyclicity at the ultra-slow spreading Southwest Indian Ridge: Evidence from variations of axial volcanic ridge morphology and abyssal hills pattern. *Geochemistry Geophysics Geosystems* 5(4) (2003).
23. Zhao, M., Qiu, X., Li, J., Sauter, D., Ruan, A., Chen, J., Cannat, M., Singh, S., Zhang, J. & Wu, Z. Three-dimensional seismic structure of the Dragon Flag oceanic core complex at the ultraslow spreading Southwest Indian Ridge (49°39'E). *Geochemistry Geophysics Geosystems* 14(10), 4544–4563 (2013).
24. Niu, X., Ruan, A., Li, J., Minshull, T.A., Sauter, D., Wu, Z., Qiu, X., Zhao, M., Chen, Y.J. and Singh, S. Along-axis variation in crustal thickness at the ultraslow spreading Southwest Indian Ridge (50°E) from a wide-angle seismic experiment. *Geochemistry Geophysics Geosystems* 16(2), 468–485 (2015).
25. Yu, Z., Li, J., Niu, X., Nicholas, R., Aiguo, R., Wang, W., Hao, H., Wei, X., Jie, Z. and Liang, Y. Lithospheric Structure and Tectonic Processes Constrained by Microearthquake Activity at the Central Ultraslow-Spreading Southwest Indian Ridge (49.2° to 50.8°E). *Journal of Geophysical Research Solid Earth* 123(8), 6247–6262 (2018).
26. Liu, C., Li, J., Tao, C., Fan, Q. & Feng, B. Variations in faulting style of the Southwest Indian Ridge (46°-53.5°E): Implications for crustal accretion process at ultraslow-spreading ridges.

- Tectonophysics 790, 228552 (2020).
27. Buck, W.R., Lavier, L.L. & Poliakov, A.N. Modes of faulting at mid-ocean ridges. *Nature* 434(7034), 719–723 (2005).
 28. Olive, J., Behn, M.D. & Tucholke, B.E. The structure of oceanic core complexes controlled by the depth distribution of magma emplacement. *Nature Geoscience* 3(7), 491–495 (2010).
 29. Tucholke, B.E., Behn, M.D., Buck, W.R. & Lin, J. Role of melt supply in oceanic detachment faulting and formation of megamullions. *Geology* 36(6), 455–458 (2008).
 30. Reston, T.J., Weinrebe, W., Grevemeyer, I., Flueh, E.R. & Kopp, H. A rifted inside corner massif on the Mid-Atlantic Ridge at 5°S. *Earth & Planetary Science Letters* 200(3), 255–269 (2002).
 31. Tao, C., Lin, J., Guo, S., Chen, Y.J., Wu, G., Han, X., German, C.R., Yoerger, D.R., Zhou, N., Li, H., Su, X., Zhu, J. & Parties, A.T. First active hydrothermal vents on an ultraslow-spreading center: Southwest Indian Ridge. *Geology* 40(1), 47–50 (2012).
 32. Zhu, J., Lin, J., Chen, Y.J., Tao, C., German, C.R., Yoerger, D.R. & Tivey, M.A. A reduced crustal magnetization zone near the first observed active hydrothermal vent field on the Southwest Indian Ridge. *Geophysical Research Letters* 37(18) (2010).
 33. Heidbach, O., Tingay, M., Barth, A., Reinecker, J., Kurfe, D. & Müller, B. Global crustal stress pattern based on the World Stress Map database release 2008. *Tectonophysics* 482(1–4), 3–15 (2010).
 34. Mckenzie, D.P. The relation between fault plane solutions for earthquakes and the directions of the principal stresses. *Bulletin of the Seismological Society of America* 59(2), 591–601 (1969).
 35. Zoback, M.L. First- and Second-Order Patterns of Stress in the Lithosphere: The World Stress Map Project. *Journal of Geophysical Research Solid Earth* 97, 11703–11728 (1992).
 36. Dziewonski, A.M., Chou, T.A. & Woodhouse, J.H. Determination of earthquake source parameters from waveform data for studies of global and regional seismicity. *Journal of Geophysical Research Solid Earth* 86(B4), 2825–2852 (1981).
 37. Ekström, G., Nettles, M. & Dziewoński, A.M. The global CMT project 2004–2010: Centroid-moment tensors for 13,017 earthquakes. *Physics of the Earth and Planetary Interiors* 200–201, 1–9 (2012).
 38. Sauter, D., Mendel, V., Rommevaux-Jestin, C., Parson, L.M., Fujimoto, H., Mével, C., Cannat, M. & Tamaki, K. Focused magmatism versus amagmatic spreading along the ultra-slow spreading Southwest Indian Ridge: Evidence from TOBI side scan sonar imagery. *Geochemistry Geophysics Geosystems* 5(10) (2004).
 39. Xu, Y., Chen, N., Tao, C., Chen, J. & Gao, B. Magmato-tectonic mechanism of Southwest Indian Ridge (49°-50°E) inferred from quantitative morphotectonic analysis based on high-resolution multibeam bathymetry. *Marine Geology* 434, 106421 (2021).
 40. Rona, P. & Gray, D. Structural behavior of fracture zones symmetric and asymmetric about a spreading axis: Mid-Atlantic Ridge (latitude 23°N to 27°N). *GSA Bulletin* 91(8), 485–494 (1980).
 41. Searle, R.C. & Laughton, A.S. Sonar studies of the Mid Atlantic Ridge and Kurchatov Fracture Zone. *Journal of Geophysical Research* (1896–1977) 82(33), 5313–5328 (1977).

42. Purdy, G.M., Sempere, J.C., Schouten, H., Dubois, D.L. & Goldsmith, R. Bathymetry of the mid-atlantic ridge, 24°-31°N: A map series. *Marine Geophysical Researches* 12(4), 247–252 (1990).
43. Eason, D.E., Dunn, R.A., Pablo, C.J. & Sohn, R.A. Segment-scale variations in seafloor volcanic and tectonic processes from multibeam sonar imaging, Mid-Atlantic Ridge Rainbow region (35°45'-36°35'N). *Geochemistry Geophysics Geosystems* 17(9), 3560–3579 (2016).
44. Howell, S.M., Olive, J., Ito, G., Behn, M.D., Escartín, J. & Kaus, B. Seafloor expression of oceanic detachment faulting reflects gradients in mid-ocean ridge magma supply. *Earth & Planetary Science Letters* 516, 176–189 (2019).
45. Escartín, J. & Lin, J. Ridge offsets, normal faulting, and gravity anomalies of slow spreading ridges. *Journal of Geophysical Research Solid Earth*. American Geophysical Union, 100 (B4), pp.6163–6177 (1995).
46. Spencer, S., Smith, D.K., Cann, J.R., Lin J. & McAllister, E. Structure and Stability of Non-Transform Discontinuities on the Mid-Atlantic Ridge between 24° N and 30° N. *Marine Geophysical Researches* 19(4), 339–362 (1997).
47. Paulatto, M., Canales, J.P, Dunn, R.A. & Sohn, R.A. Heterogeneous and asymmetric crustal accretion: New constraints from multibeam bathymetry and potential field data from the Rainbow area of the Mid-Atlantic Ridge (36°15'N). *Geochemistry Geophysics Geosystems* 16(9), 2994–3014 (2015).
48. Tivey, M. A., Schouten, H., & Kleinrock, M. C. A near-bottom magnetic survey of the Mid-Atlantic Ridge axis at 26°N: Implications for the tectonic evolution of the TAG segment. *Journal of Geophysical Research*, 108(B5), 2277 (2003).
49. Canales, J. P., Sohn, R. A. & DeMartin, B. J. Crustal structure of the Trans-Atlantic Geotraverse (TAG) segment (Mid-Atlantic Ridge, 26°10'N): Implications for the nature of hydrothermal circulation and detachment faulting at slow spreading ridges. *Geochemistry, Geophysics, Geosystems*, 8, Q08004 (2007).
50. Baker, E.T. & German, C.R. On the global distribution of mid-ocean ridge hydrothermal vent-fields. *American Geophysical Union*, pp. 245–266 (2004).
51. Fisher and Andrew, T. Permeability within basaltic oceanic crust. *Reviews of Geophysics* 36(2), 143–182 (1998).
52. German, C.R., Parson, L.M., Bougault, H., Coller, D., Critchley, M., Dapoigny, A., Day, C. & Eardley, D. Hydrothermal exploration near the Azores Triple Junction: tectonic control of venting at slowspreading ridges? *Earth & Planetary Science Letters* 139,93–104 (1996).
53. Babeshko, VA., Evdokimova, O.V. & Babeshko, O.M. On the possibility of predicting some types of earthquake by a mechanical approach. *Acta Mechanica* 229(5), 2163–2175 (2018).
54. Zhou, J. & Li, D. Numerical analysis of coupled water, heat and stress in saturated freezing soil. *Cold Regions Science and Technology* 72, 43–49 (2012).
55. Dyksterhuis, S., Müller, R.D. & Albert, R.A. Paleostress field evolution of the Australian continent since the Eocene. *Journal of Geophysical Research Solid Earth* 110(B5) (2005).

56. Hyndman, R.D. & Drury, M.J. The physical properties of oceanic basement rocks from deep drilling on the Mid-Atlantic Ridge. *Journal of Geophysical Research* 81(23), 4042–4052 (1976).
57. Tao, C., Tao, W.U., Jin, X., Dou, B., Huaiming, L. & Zhou, J. Petrophysical characteristics of rocks and sulfides from the SWIR hydrothermal field. *Acta Oceanologica Sinica* 32(12), 118–125 (2013).
58. Brocher, T.M. Empirical Relations between Elastic Wavespeeds and Density in the Earth's Crust. *Bulletin of the Seismological Society of America* 95(6), 2081–2092 (2005).

Tables

Tables 1 and 2 are available in the Supplementary Files section.

Figures

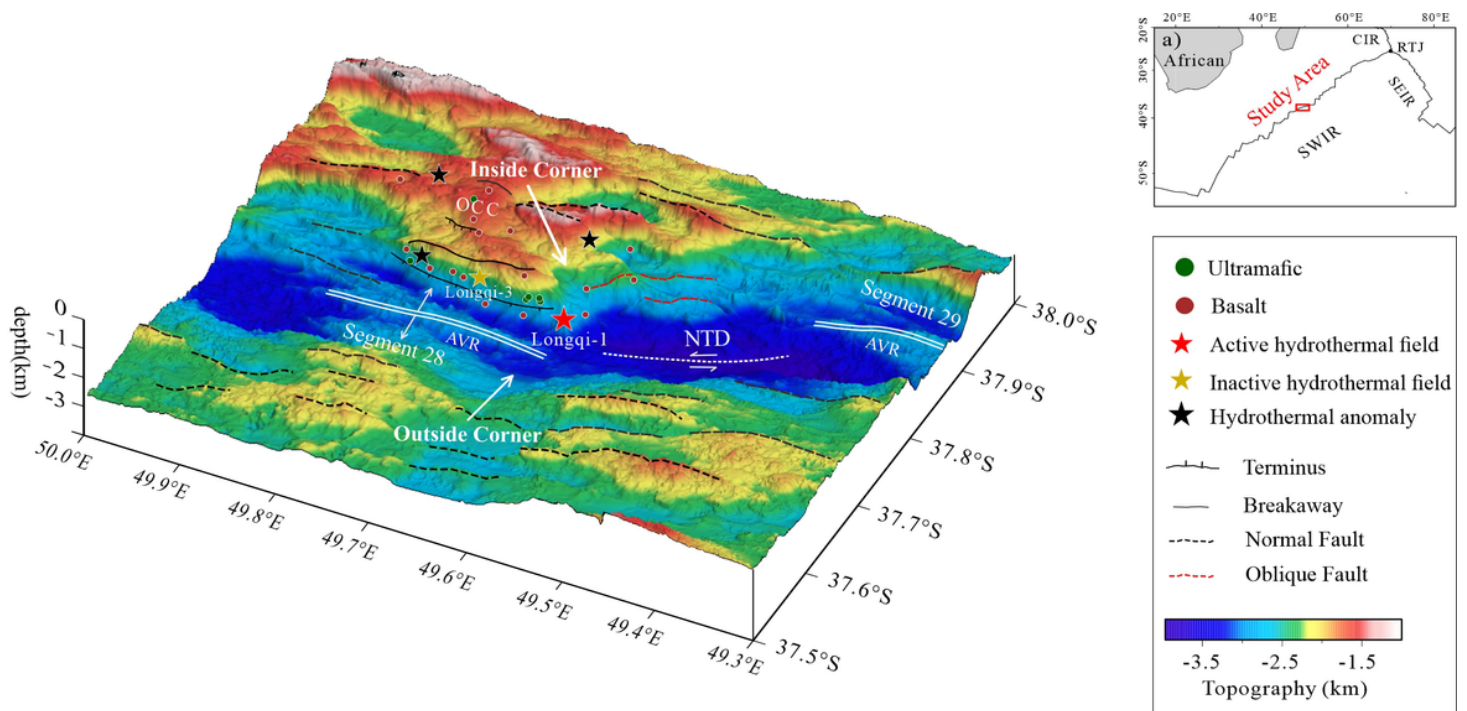


Figure 1

Legend not included with this version.

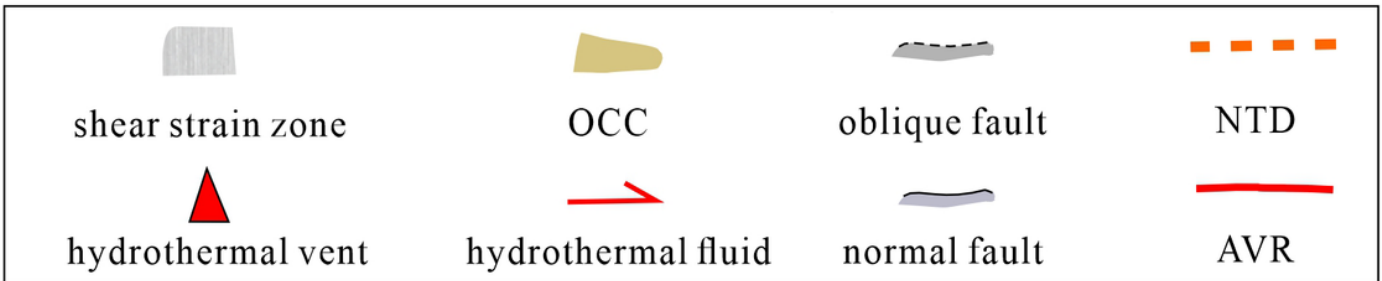
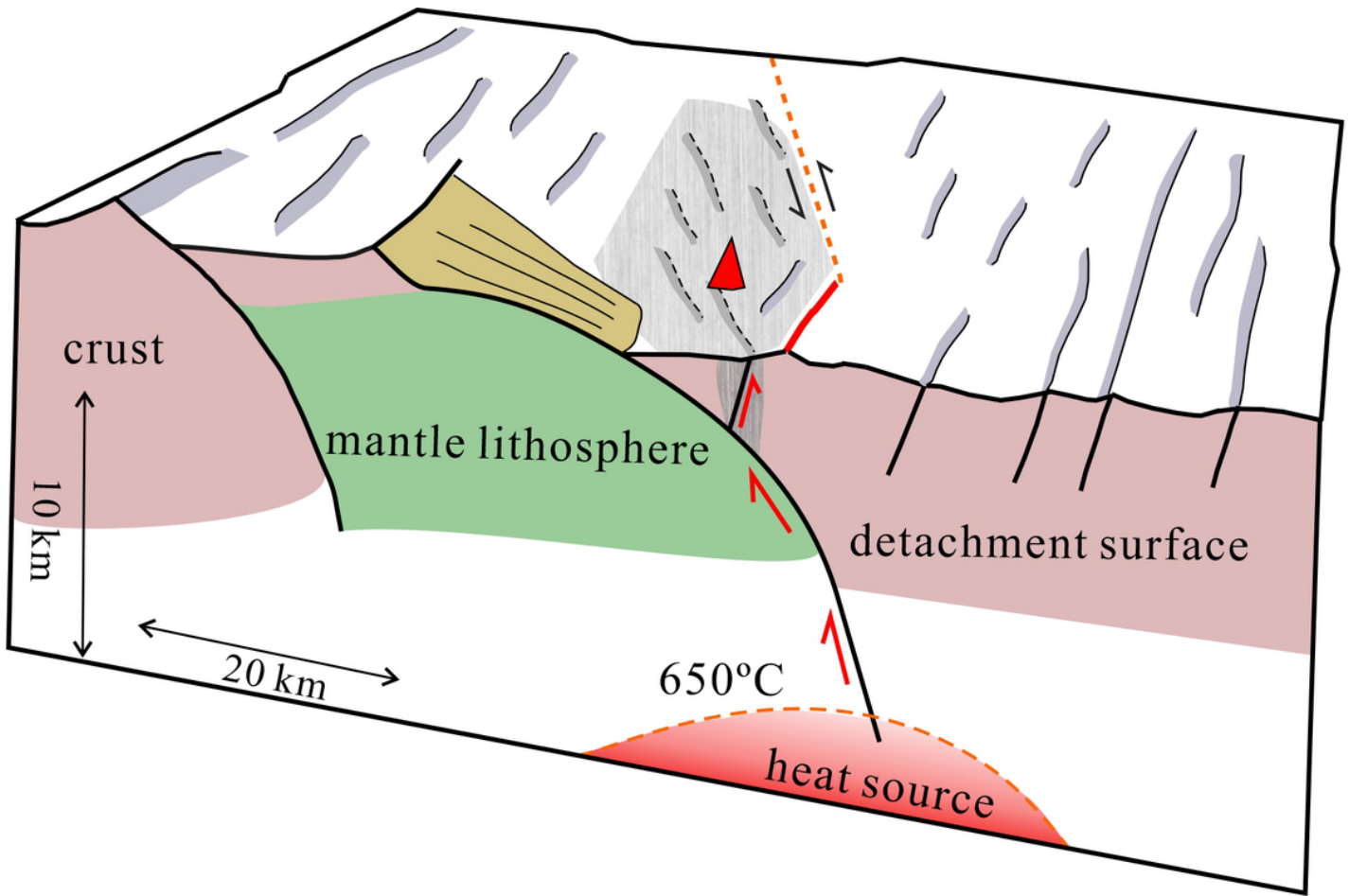


Figure 2

Legend not included with this version.

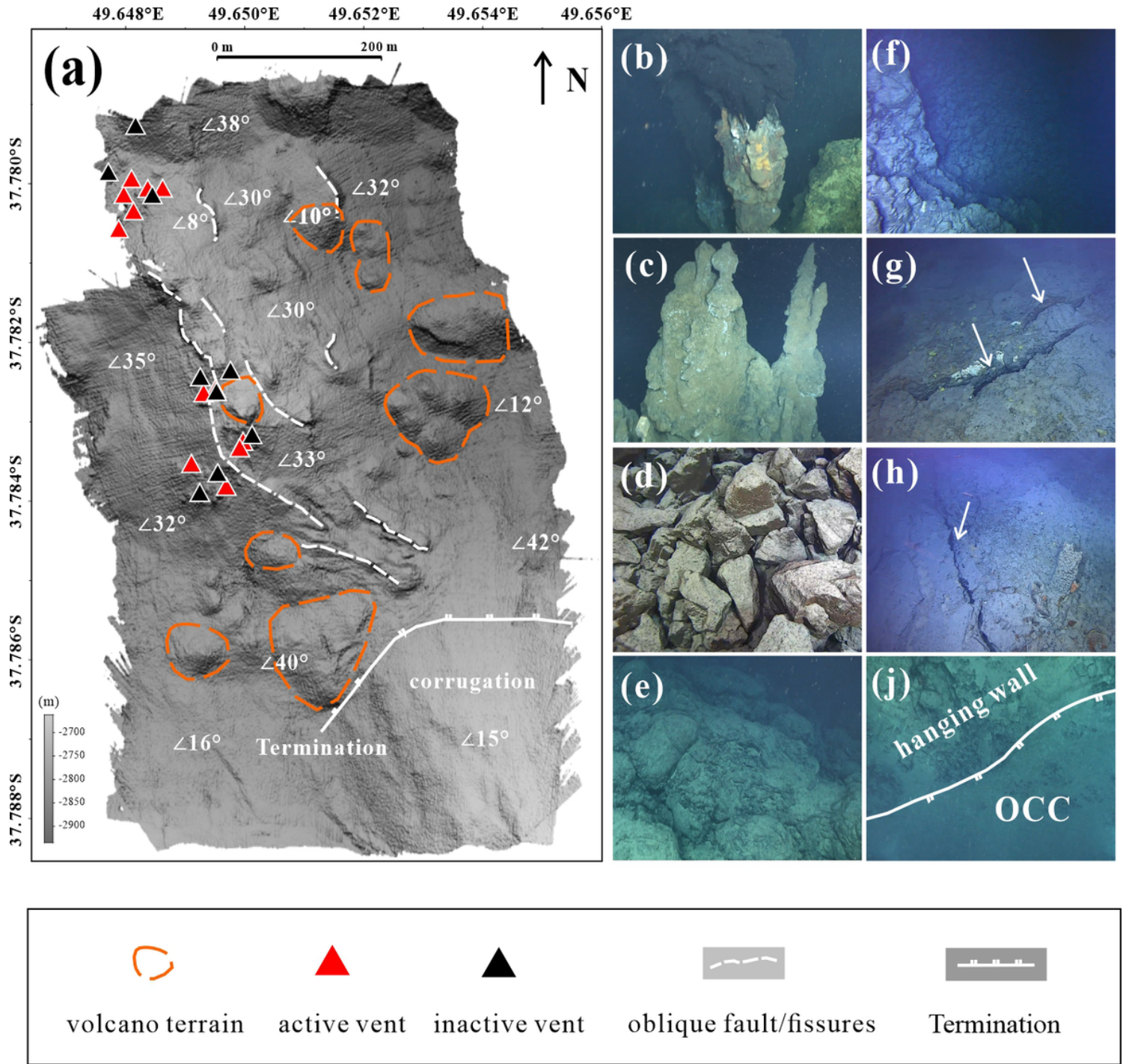


Figure 3

Legend not included with this version.

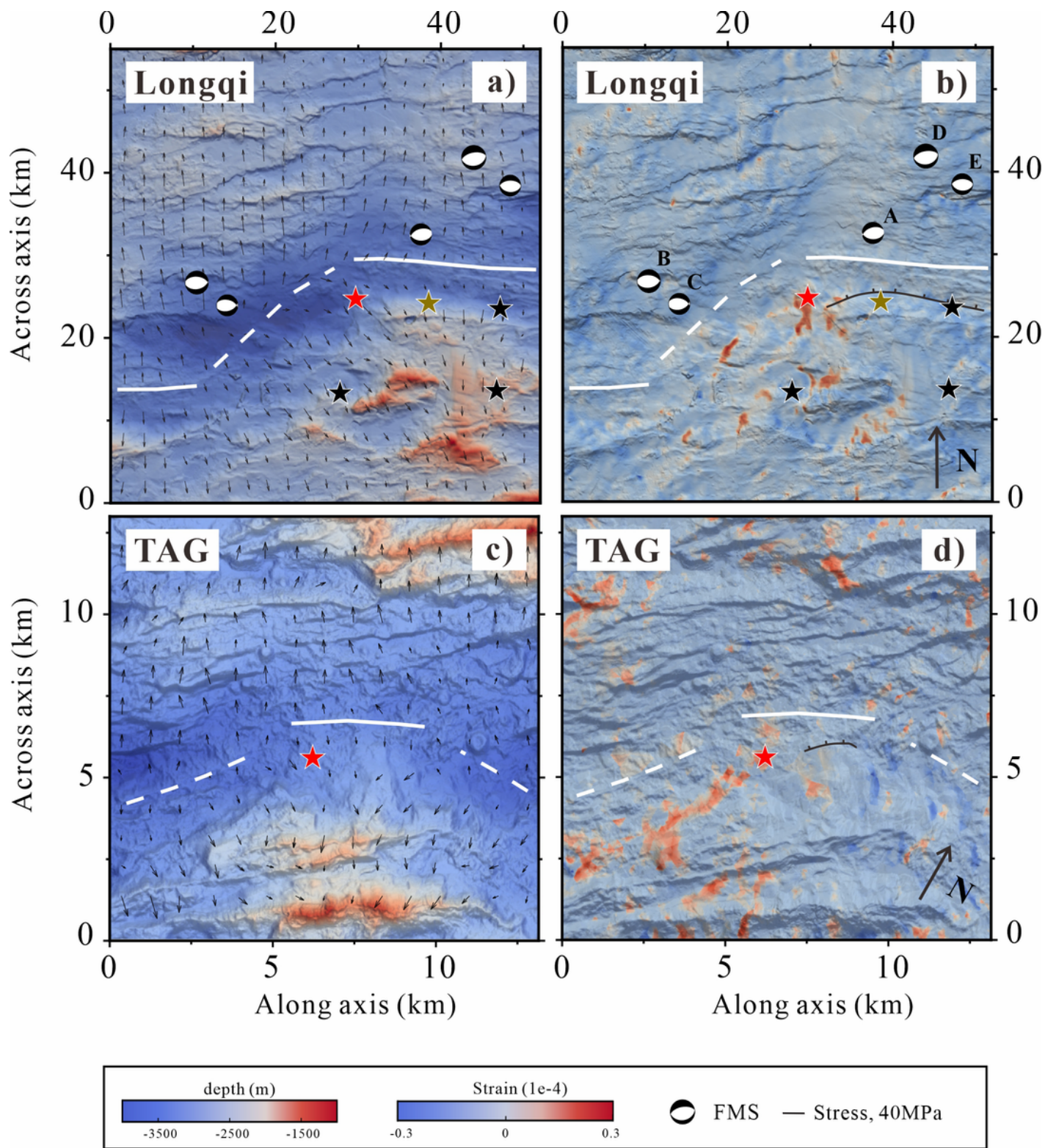


Figure 4

Legend not included with this version.

Supplementary Files

This is a list of supplementary files associated with this preprint. Click to download.

- [SupplementaryMaterials.pdf](#)